The Astrophysical Journal, 609:378–391, 2004 July 1

FAR-ULTRAVIOLET SPECTROSCOPIC ANALYSES OF FOUR CENTRAL STARS OF PLANETARY NEBULAE[1]

J. E. Herald and L. Bianchi
Department of Physics and Astronomy, The Johns Hopkins University, 3400 North Charles Street, Baltimore, MD 21218-2411
Received 2003 December 23; accepted 2004 March 15

ABSTRACT

We analyze the far-UV/UV spectra of four central stars of planetary nebulae (CSPNs) with strong wind features—NGC 2371, A78, IC 4776, and NGC 1535—and derive their photospheric and wind parameters by modeling high-resolution *FUSE* (*Far Ultraviolet Spectroscopic Explorer*) data in the far-UV and *HST* (*Hubble Space Telescope*) STIS and *IUE* data in the UV with spherical, non-LTE, line-blanketed model atmospheres. A78 is a hydrogen-deficient transitional [WR]-PG 1159 object, and we find NGC 2371 to be in the same stage, both migrating from the constant-luminosity phase to the white dwarf cooling sequence, with $T_{\rm eff} \simeq 120$ kK, $\dot{M} \simeq 5 \times 10^{-8}\ M_{\odot}\ {\rm yr}^{-1}$. NGC 1535 is a "hydrogen-rich" O(H) CSPN, and the exact nature of IC 4776 is ambiguous, although it appears to be helium-burning. Both objects lie on the constant-luminosity branch of post-AGB evolution and have $T_{\rm eff} \simeq 65$ kK, $\dot{M} \simeq 1 \times 10^{-8}\ M_{\odot}\ {\rm yr}^{-1}$. Thus, both the H-rich and H-deficient channels of PN evolution are represented in our sample. We also investigate the effects of including higher ionization stages of iron (up to Fe x) in the model atmosphere calculations of these hot objects (usually neglected in previous analyses) and find iron to be a useful diagnostic of the stellar parameters in some cases. The far-UV spectra of all four objects show evidence of hot ($T \sim 300$ K) molecular hydrogen in their circumstellar environments.

Subject headings: planetary nebulae: general — stars: atmospheres — stars: individual (A78, IC 4776, NGC 1535, NGC 2371) — stars: Wolf-Rayet —ultraviolet: stars

On-line material: color figures

1. INTRODUCTION

After leaving the asymptotic giant branch (AGB), low- and intermediate-mass stars become central stars of planetary nebulae (CSPNs). The spectral types of the central stars are numerous and diverse (e.g., O, Of, sdO, [WR] (Wolf-Rayet), and [WR]–PG 1159, as well as white dwarf types), but all of these can be generally divided into two groups based on surface abundances: hydrogen-rich (which show obvious hydrogen lines in their spectra) and hydrogen-deficient (which do not). H-deficient stars are in a post–helium flash, helium-burning phase, while the H-rich stars may be either hydrogen- or helium-burning. About 10%–20% of CSPNs are H-deficient (De Marco & Soker 2002; Koesterke & Werner 1998 and references therein). The two groups are thought to represent different "channels" of CSPN evolution, terminating with either H-rich DA-type or He-rich DO-type white dwarfs (e.g., Napiwotzki 1999). During the CSPN phase the star sheds mass in the form of a stellar wind as it evolves toward the white dwarf cooling sequence. It is generally believed that the winds of these objects are driven by radiation pressure, as with Population I O stars and WR stars. If the driving of the wind is mainly dictated by the stellar luminosity, the wind parameters can, in principle, be used to determine the distances to CSPNs (Kudritzki et al. 1999; Kudritzki & Puls 2000; Tinkler & Lamers 2002).

The spectra of the majority of the H-deficient class have strong wind signatures, show no photospheric lines, and are very similar to those of WC stars—the carbon-rich WR stars, which are evolved massive stars. The low-mass central stars are termed "[WC]" stars to denote their association with planetary nebulae. "PG 1159–type" stars are extremely hot, H-deficient, white dwarf–type objects, thought to represent an entry point onto the white dwarf cooling sequence. They show mainly absorption lines in the optical spectra but possess a few wind lines in the UV. Because PG 1159 objects have abundances similar to those of [WC] stars and about half of the PG 1159 stars are CSPNs (Werner 2001), they are thought to be descendants of the [WC] stars. Linking these two classes is a rare group of objects named "[WC]–PG 1159" stars, whose spectra show both emission lines and some absorption lines. Only three definite cases of such stars are known so far: A78, A30, and Longmore 4 (Koesterke 2001). Parthasarathy et al. (1998) have posited that all "weak emission line stars" (WELSs) are actually [WC]–PG 1159 stars, on the basis of optical spectra, but Werner (2001) cautioned against this statement until better spectra of the sample is available. The H-rich CSPNs of Méndez et al. (1988) are similar in that their spectra also feature absorption lines as well as UV wind emission features.

[WC], [WC]–PG 1159, and PG 1159 stars all reside in the same area of the H-R diagram (HRD). In terms of evolution, this region corresponds to the bend where the star leaves the constant-luminosity, post-AGB phase and is in transition to the white dwarf cooling sequence. [WC] and PG 1159 stars lie close to each other in the HRD, yet have very different spectra (in the optical, a [WC] spectrum is littered with strong emission lines, while that of a PG 1159 star presents an absorption-line spectrum). This suggests a dramatic drop in mass-loss rates over a short time of evolution (Koesterke & Werner 1998). The commonly accepted evolutionary sequence for H-deficient CSPNs is [WC] → [WC]–PG 1159 → PG 1159 → DO WD (Hamann 1996). This sequence spans the time when the stellar

[1] Based on observations made with the NASA-CNES-CSA *Far Ultraviolet Spectroscopic Explorer* (*FUSE*) and data from the MAST archive. *FUSE* is operated for NASA by the Johns Hopkins University, under NASA contract NAS5-32985.

TABLE 1
THE PROGRAM OBJECTS

Name	PN G	R.A. (J2000.0)	Decl. (J2000.0)	v_r[a] (km s^{-1})	PN Diameter (arcsec)
NGC 2371	189.1+19.8	07 25 34.71	+29 29 26.20	$+20.6 \pm 2.7$	48.9×30.6[b]
A78	081.2−14.9	21 35 29.8	+31 41 40	$+17 \pm 10.0$	107[a]
NGC 1535	206.4−40.5	04 14 15.9	−12 44 21	-3.2 ± 1.4	33.3×32.1[b]
IC 4776	002.0−13.4	18 45 50.57	−33 20 32.94	$+18.9 \pm 0.7$	8.5×4.0[b]

NOTE.—Units of right ascension are hours, minutes, and seconds, and units of declination are degrees, arcminutes, and arcseconds.
[a] Cahn & Kaler (1971).
[b] Tylenda et al. (2003); two dimensions given.

winds are in the process of "turning off." Therefore, understanding the objects in this part of the HRD is not only a prerequisite for understanding the evolution of central stars but will also give insight into the driving of stellar winds in general.

In the classification of [WR]-type objects, wind parameters are more fundamental discriminators than stellar temperature (Crowther 1999; Acker & Neiner 2003). As the central star's winds die down, the wind features in the FUV/UV are the last to fade (Koesterke et al. 1998). Therefore, to estimate accurate parameters of the extended atmospheres, this phase is best studied in the FUV/UV. In this paper, we present an FUV/UV–based spectral analysis of four CSPNs that show strong wind signatures—NGC 2371, A78, IC 4776, and NGC 1535. We model the FUV/UV spectra of these stars using stellar atmospheres codes to determine the wind parameters, such as $T_{\rm eff}$, $\dot{M}$, and v_∞, and discuss their evolutionary implications. A78 has been classified as a [WO]–PG 1159 transition object (Méndez 1991; Crowther et al. 1998), and we argue that NGC 2371 also belongs to this class. NGC 1535 is an O(H) star belonging to the H-rich sample of Méndez et al. (1988). The FUV spectra of IC 4776 is similar to that of NGC 1535, but we find evidence that this object may be an He burner. Comparing with evolutionary calculations, our derived parameters place the latter two objects along the constant-luminosity path of the HRD, while the former two lie on the bend marking the transition from that phase to the white dwarf cooling sequence.

This paper is arranged as follows. The observations and data reduction are described in § 2. A comparison of the spectra of the objects is presented in § 3. Our models and parameter determinations are described in § 4. The implications of our results are discussed in § 5 and our conclusions in § 6.

2. OBSERVATIONS AND REDUCTION

The coordinates, radial velocities (v_r), and nebular diameters (θ) of our four sample objects are listed in Table 1 (Tylenda et al. 2003 have measured two angular dimensions for three of the sample PNs, corresponding to the semimajor and semiminor diameters, which we list as $\theta_B \times \theta_A$). The data sets utilized in this paper are summarized in Table 2. NGC 2371 and IC 4776 were observed as part of *FUSE* cycle 1 program P133 (PI Bianchi). All other FUV/UV data were retrieved from the MAST archive, including *FUSE* and STIS archive data of NGC 1535, a Berkeley Extreme and Far-UV Spectrometer (BEFS) archive spectrum of A78, and *IUE* data of most objects. The reduction of the *FUSE* data is described in § 2.1.

2.1. *FUV Data*

FUSE covers the wavelength range of 905–1187 Å at a spectral resolution of $\lesssim$30,000. It is described by Moos et al. (2000), and its on-orbit performance is discussed by Sahnow et al. (2000). *FUSE* collects light concurrently in four different channels (LiF1, LiF2, SiC1, and SiC2). Each channel is recorded by two detectors, each divided into two segments (A and B) covering different subsets of the above range, with some overlap.

The *FUSE* spectra were taken using the LWRS ($30'' \times 30''$) aperture. These data, taken in "time tag" mode, have been calibrated using the most recent *FUSE* data reduction pipeline, efficiency curves, and wavelength solutions (CALFUSE, ver. 2.2). We combined the data from different segments, weighting by detector sensitivity, and rebinned them to a uniform dispersion of 0.05 Å (which is probably close to the actual resolution, since the data were taken in the early part of the mission). Bad areas of the detectors and those regimes affected

TABLE 2
UTILIZED SPECTRA

Star	Instrument	Data Set	Date	Resolution (Å)	Aperture (arcsec)	Range (Å)	Scale Factor
NGC 2371	*FUSE*	P1330301	2000 Feb 26	~0.05	30×30	915–1180	...
	IUE	SWP04883	1979 Apr 7	5–6	10×20	1180–1975	1.3
	IUE	LWR04210	1979 Apr 7	5–6	10×20	1975–3345	1.3
A78	BEFS	BEFS2190	1996 Dec 1	~0.33	20	915–1222	...
	IUE	SWP19906	1983 May 5	~0.2	10×20	1122–1975	1.2
NGC 1535	*FUSE*	P1150808	2001 Oct 5	~0.05	30×30	915–1180	...
	STIS+E140M	O64D04010	2001 Mar 1	~0.05	0.2×0.2	1180–1700	...
IC 4776	*FUSE*	P1330501	2000 May 21	~0.05	30×30	915–1180	...
	IUE	SWP16504	1982 Mar 11	5–6	10×20	1180–1975	1.25
	IUE	LWR12764	1982 Mar 11	5–6	10×20	1975–3345	1.25

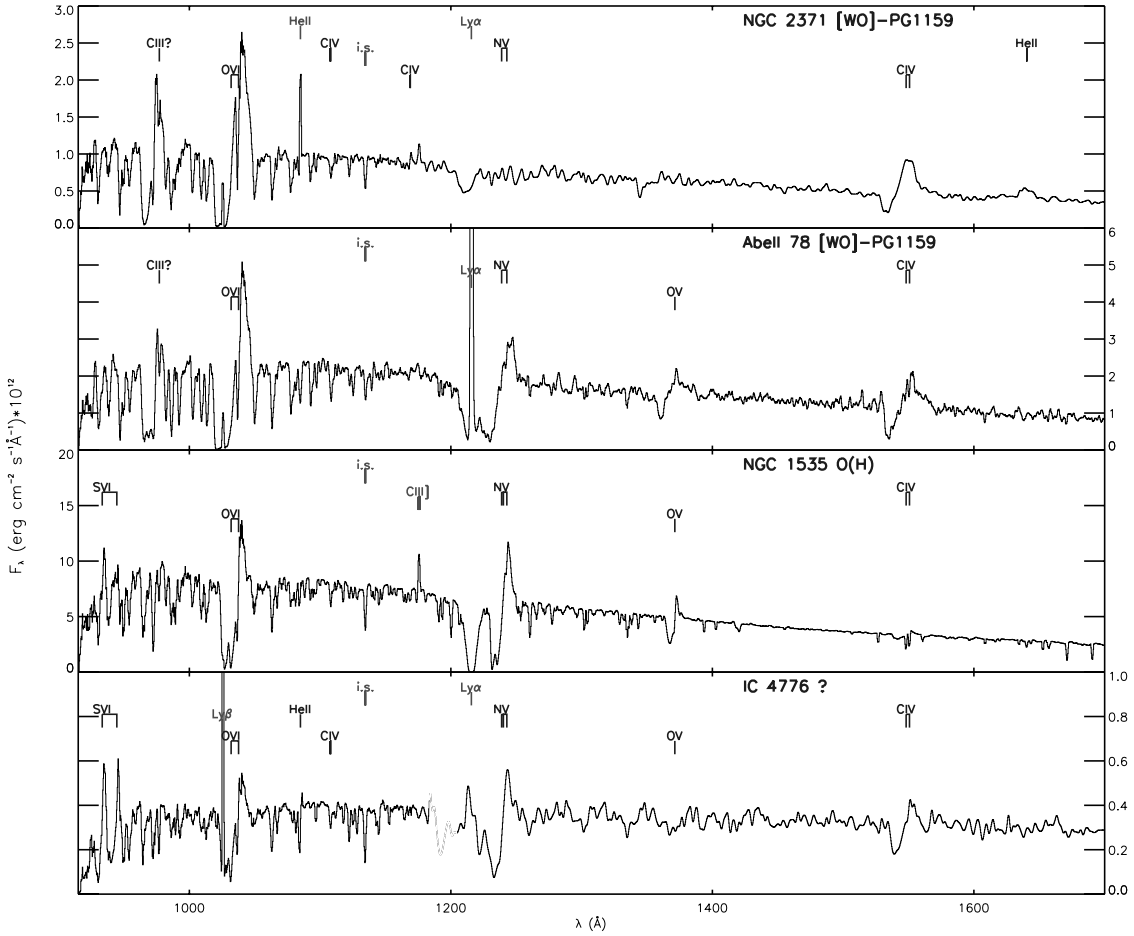

FIG. 1.—FUV/UV spectra of our sample. Data are from different instruments (with different resolutions; see Table 2). The spectrum of IC 4776 appears flatter than the others because of the contribution from the nebular continuum (see § 4.3). Prominent stellar features are marked with dark labels, and interstellar/nebular features by light labels. Regions of bad data are blanked out. [*See the electronic edition of the Journal for a color version of this figure.*]

by an instrumental artifact known as "the worm" (*FUSE* Data Handbook, ver. 1.1) were excluded. The flux calibration accuracy of *FUSE* is $\lesssim$10% (Sahnow et al. 2000).

The BEFS spectra cover a wavelength range of 912–1218 Å with a resolution of $\sim$0.33 Å. The calibration and performance are described by Hurwitz et al. (1998).

2.2. *UV Data*

For most stars, we make use of *IUE* data, using high-resolution spectra if available (a high-resolution spectrum for NGC 2371 exists but is of poor quality, so we present the low-resolution data instead). For some stars, there was some disagreement ($\lesssim$30%) between the FUV (both *FUSE* and BEFS) and *IUE* continuum levels in the regions of overlap (flux calibrations for these instruments are typically accurate to $\sim$10%). Because there are no nearby objects that could contribute extra flux in the *FUSE* aperture, we suspect that the background has been oversubtracted in the *IUE* spectra, since nebular continuum emission is expected (in the case of NGC 1535, the STIS spectra agree perfectly well with the *FUSE* fluxes, but the *IUE* fluxes are a factor of $\sim$1.2 lower). Therefore, we have scaled the UV flux levels to those of the FUV (scaling factors are listed in Table 2).

3. DESCRIPTION OF THE SPECTRA

Figure 1 displays the combined FUV/UV spectra of our sample (up to 1700 Å; longward of this, the spectra are mostly featureless). Much of the fine structure between 900 and 1200 Å is caused by sight-line molecular hydrogen (H_2) and is discussed in § 4.2. As far as stellar features go, the spectra present a sparse landscape. The O VI $\lambda\lambda$1032–1038 feature is most prominent in all cases, and the spectra are arranged from top to bottom in order of decreasing strength of this feature. IC 4776 and NGC 1535 both display S VI $\lambda\lambda$933–944 in the FUV; however, their UV spectra are different. In the FUV, A78 and NGC 2371 have three similar lines, but N V $\lambda\lambda$1238–1243 and O V λ1371 are strong P Cygni features in A78 while absent in NGC 2371; neither star shows S VI, but both display a P Cygni feature around 977 Å. This feature is commonly assumed to be C III; however, the formation of a C III line in the highly ionized winds of these objects is hard to explain, and this is discussed in § 5.

C IV $\lambda\lambda$1548–1551 appears in all spectra, although it is relatively weak in NGC 1535. N V $\lambda\lambda$1238–1243 is obviously present in all spectra save that of NGC 2371. O V λ1371 is absent in NGC 2371, is present as a P Cygni profile in A78 and NGC 1535, and appears perhaps only in absorption in IC 4776. He II λ1640 appears to be present in the low-resolution *IUE* spectrum of NGC 2371, but inspection of the one available (noisy) high-resolution *IUE* spectra for this object (SWP53006) shows the He II λ1640 to be at least partly nebular in origin. The absence of transitions from ions of lower ionization potential (e.g., N IV, O IV, or Si IV) indicates the high ionization state of the winds and high effective temperatures of the central stars.

4. MODELING

The modeling of these spectra consists of three parts: the central star spectrum, the nebular continuum emission longward of 1200 Å, and the sight-line hydrogen (atomic and molecular) absorption shortward of 1200 Å. The reddening must also be adjusted concurrently to match the FUV/UV slope. In all four objects, the reddening is low and not a significant source of uncertainty. Iterations between each are required to achieve a consistent solution. However, we discuss each in turn for clarity.

4.1. *The Central Stars*

The optical spectra of these objects show mainly absorption lines, and some have been modeled using plane-parallel codes (e.g., A78 by Werner et al. 2003; NGC 1535 by Méndez et al. 1988). In the FUV/UV, the most prominent features are wind lines. The temperatures and wind parameters of some of these objects have been previously determined from plane-parallel analyses, in conjunction with wind-line analyses of one or two wind features (such as C IV $\lambda\lambda$1548–1551 or O VI $\lambda\lambda$1332–1338; Koesterke & Werner 1998). Here we derive wind parameters solely from the FUV/UV spectra.

Intense radiation fields, a (relatively) low wind density, and an extended atmosphere invalidate the assumptions of thermodynamic equilibrium and a plane-parallel geometry for the winds of our sample CSPNs. To model these winds, we use the non-LTE (NLTE), line-blanketed code CMFGEN of Hillier & Miller (1998, 1999). CMFGEN solves the radiative transfer equation in an extended, spherically symmetric, expanding atmosphere. Originally developed to model the WR winds, it has been adapted for objects with weaker winds, such as O stars and CSPNs, as described in Hillier et al. (2003). The detailed workings of the code are explained in the references therein. To summarize, the code solves for the NLTE populations in the comoving frame of reference. The fundamental photospheric/wind parameters include $T_{\rm eff}$, R_*, $\dot{M}$, the elemental abundances, and the velocity law (including v_∞). The *stellar radius* (R_*) is taken to be the inner boundary of the model atmosphere (corresponding to a Rosseland optical depth of $\sim$20). The temperature at different depths is determined by the *stellar temperature* T_*, related to the luminosity and radius by $L = 4\pi R_*^2 \sigma T_*^4$, whereas the *effective temperature* ($T_{\rm eff}$) is similarly defined, but at a radius corresponding to a Rosseland optical depth of 2/3 ($R_{2/3}$). The luminosity is conserved at all depths, so $L = 4\pi R_{2/3}^2 \sigma T_{\rm eff}^4$.

The terminal velocity (v_∞) can be estimated from the blue edge of the P Cygni absorption features, preferably from features that extend farther out in the wind (we used C IV $\lambda\lambda$1548–1551 primarily). We assume what is essentially a standard velocity law $v(r) = v_\infty(1 - r_0/r)^\beta$, where r_0 is roughly equal to R_*. Once a velocity law is specified, the density structure of the wind is then parameterized by the mass-loss rate through the equation of continuity: $\dot{M} = 4\pi R_*^2 \rho(r) v(r)$.

It has been found that models with the same *transformed radius* R_t [$\propto R_* \left(v_\infty/\dot{M}\right)^{2/3}$] (Schmutz et al. 1989) and v_∞ have the same ionization structure, temperature stratification (aside from a scaling by R_*), and spectra (aside from a scaling of the absolute flux by R_*^2; Schmutz et al. 1989; Hamann et al. 1993). Thus, once the velocity law and abundances are set, one parameter may be fixed (e.g., R_*), and parameter space can then be explored by varying only the other two parameters (e.g., $\dot{M}$ and $T_{\rm eff}$). Here R_t can be thought of as an optical depth parameter, because the optical depth of the wind scales as $\propto R_t^{-3}$, for opacities that are proportional to the square of the density. Scaling the model to the observed flux yields R_*/D—a distance D must be adopted to determine R_*.

For the model ions, CMFGEN utilizes the concept of "superlevels," whereby levels of similar energies are grouped together and treated as a single level in the rate equations (Hillier & Miller 1998). Ions and the number of levels and superlevels included in the model calculations, as well references to the atomic data, are given in the Appendix.

4.1.1. *Clumping*

Radiation-driven winds have been shown to be inherently unstable (Owocki et al. 1988, 1994), which should lead to the formation of clumps in the expanding atmosphere. The degree of clumpiness is parameterized by f, the *filling factor*. One actually can only derive $\dot{M}_{\rm sm} = \left(\dot{M}_{\rm cl}/\sqrt{f}\right)$ from the models, where $\dot{M}_{\rm sm}$ and $\dot{M}_{\rm cl}$ are the smooth and clumped mass-loss rates. For the denser winds of Population I WR stars, the clumping factor can be constrained by the strength of the electron-scattered optical line wings, and clumping factors of $f \sim 0.1$ are typical (a reduction of $\dot{M}$ to roughly a third of its smooth value). For O stars, the lower mass-loss rates make the electron-scattering effects small and difficult to constrain (Hillier et al. 2003). The winds of our sample stars are even weaker, and we do not attempt to determine the clumping for our sample. Unless otherwise noted, we have adopted $f = 1$ and use $\dot{M}$ to refer to the smooth mass-loss rate throughout this paper. This can be seen as an upper limit, with a conservative estimate of the lower limit of $\dot{M}$ being a third of this value.

4.1.2. *Gravity*

Because the FUV/UV range contains mostly wind lines, there are no suitable absorption lines to be used as gravity diagnostics. In CMFGEN, gravity enters through the scale height h ($\propto g^{-1}$), which connects the spherically extended hydrostatic outer layers to the wind. The relation between h and g, defined in Hillier et al. (2003), involves the mean ionic mass and the mean number of electrons per ion, the local electron temperature, and the ratio of radiation pressure to the gravity. Méndez et al. (1988) determined $\log g = 4.3 \pm 0.2$ for NGC 1535, and Werner et al. (2003) found $\log g = 5.5$ for A78 through analysis of photospheric optical lines. We initially adopted $\log g = 4.3$ for NGC 1535 and IC 4776 and $\log g = 5.5$ for A78 and NGC 2371. For such gravities, the derived wind parameters are not very sensitive to h. Spectral wind features can be fitted with models of the same $T_{\rm eff}$ but with gravities differing by over a magnitude. We discuss the issue of gravity more in § 5.

4.1.3. *Abundances*

Throughout this work, the nomenclature X_i represents the mass fraction of element i, $X_\odot$ denotes the solar abundance, and our values for solar are taken from Gray (1992).

Because of the lack of photospheric lines, we have made assumptions about the abundances of the model atmospheres. We have computed models with two different abundance patterns: solar abundance for all elements (corresponding to H-rich objects) and carbon/oxygen enriched [WC]–PG 1159–type abundances, typical of H-deficient CSPNs. With respect to the latter, it has been shown that abundances through the [WC] subclasses are about the same (Crowther et al. 2002,

TABLE 3
MODEL ABUNDANCES

Star	X_H	X_{He}	X_C	X_N	X_O	X_{Si}	X_S	X_{Fe}
NGC 2371.....	...	0.54	0.37	$\lesssim 0.01$[a]	0.08	$X_\odot$	$X_\odot$	$X_\odot$[a]
A78.....	...	0.54	0.37	0.01	0.08	$X_\odot$	$X_\odot$	$\lesssim 0.03\ X_\odot$
NGC 1535.....	$X_\odot$	$X_\odot$	$X_\odot$	$X_\odot$	$X_\odot$	$X_\odot$	$X_\odot$	$X_\odot$
IC 4776.....	$X_\odot$	$X_\odot$	$X_\odot$	$X_\odot$	$X_\odot$	$X_\odot$	$X_\odot$	$X_\odot$

NOTE.—$X_\odot$ = solar abundance.
[a] Value uncertain, see text.

1998), with the spectroscopic differences mainly tied to $\dot{M}$ and $T_{\rm eff}$ (Crowther et al. 2002). Calculations by Herwig (2001) show that these abundances may result when the star experiences a late He shell flash. The abundances of PG 1159 objects are similar (Górny & Tylenda 2000). Typical measured values are (by mass): $X_{He} = 0.33$–0.80, $X_C = 0.15$–0.50, and $X_O = 0.06$–0.17 (Werner 2001). For these reasons, we have assumed a similar abundance pattern for these elements [(X_{He}, X_C, X_O) = (0.54, 0.36, 0.08)], while adopting solar abundances for others (e.g., S, Si, and Fe). The nitrogen abundance in such objects typically ranges from undetectable to $\sim$2% (by mass; see Werner 2001 and references therein). We have adopted a nitrogen abundance of 1% for most of our models. The lone N V $\lambda\lambda$1238–1243 feature is abundance-sensitive, and we do not rely on it strongly as a diagnostic, as it is also sensitive to $T_{\rm eff}$ and $\dot{M}$. We use these abundances in our models of A78 (a [WR]–PG 1159 star) and NGC 2371, which has a similar FUV spectrum (Fig. 1).

For the H-rich O(H) star NGC 1535, we have adopted solar abundances for all elements. For IC 4776, which displays a similar FUV/UV spectrum, we have computed models with both solar abundances and the above H-deficient [WC]–PG 1159 abundances. We are able to fit its spectrum adequately with models of both abundances (we discuss this more in § 4.1.6).

Table 3 shows our final model elemental abundances. For most, our assumed abundances produced adequate fits. Some required adjusting, as described in § 4.1.6, on a case-by-case basis.

4.1.4. *Diagnostics*

Optimally, one determines $T_{\rm eff}$ by the ionization balance of He or the CNO elements. It is desirable to use diagnostics from many elements to ensure consistency. However, in the FUV/UV spectra of these objects only oxygen shows two ionization stages—O V and O VI. We find the O VI feature to be mainly insensitive to $\dot{M}$ and moderately sensitive to $T_{\rm eff}$; however, the possible influence of X-rays on this line makes it a less-than-desirable temperature diagnostic (in the O star regime, O VI is also sensitive to $\dot{M}$, but above a sharp threshold, and this line is primarily created by X-rays; Bianchi & Garcia 2002). The other elements (C, N, and S) only show one ionization stage. Because of the lack of multiple ionization stages from the same element in the spectra of most of our sample, effective temperatures are mainly derived from the appearance or absence of ions of different ionization potentials. For example, in our cooler objects (IC 4776 and NGC 1535) the absence of low-ionization features, such as S V (73 eV), P V (65 eV), O IV (77 eV), and N IV (77 eV), places a lower limit on $T_{\rm eff}$ ($\sim$55–60 kK from our models) for a wide range of mass-loss rates and abundances. Tinkler & Lamers (2002) find that between 55 and 70 kK, H-rich CSPNs exhibit a large jump in $\dot{M}$ by a factor of 10–100, which they suspect is due to a bistability jump. In our models, it is in this temperature range that these previously mentioned ions jump to the next stage, supporting the idea of Vink et al. (2001) that a bistability jump at such high temperatures may be due to CNO elements. The presence of S VI in these objects' spectra further constrains the temperature to be below a certain point. Above $T_{\rm eff} \gtrsim 90$ kK, S VII becomes dominant in the outer wind, and a regime is entered in which our "hotter" objects lie (NGC 2371 and A78). Around $T_{\rm eff} \simeq 120$ kK, the winds become too ionized for O V, a discriminator between our two hot objects.

Saturated features (like O VI) are mainly insensitive to the mass-loss rate. We typically use the observed C IV, O V, and S VI lines to constrain $\dot{M}$. In addition, He II λ1640 (not observed in most of our sample objects) is used to place upper limits on this parameter. In some cases, we also use the iron spectrum as an additional diagnostic (§ 4.1.5).

4.1.5. *Iron*

The effects of iron (and other line-blanketing elements) are important to consider in the modeling of hot stars for multiple reasons. It is known that in the modeling of hot stars, the neglect of important line-blanketing elements, such as iron, can significantly affect the derived parameters. Furthermore, iron features may be used to provide additional diagnostics of stellar parameters (e.g., Herald et al. 2001). Finally, line-blanketing elements, such as iron, are high sources of opacity in the wind and are thus important in the understanding of how it is driven.

Our sample represents an ideal test bed for studying the effects of the inclusion of higher ionization stages of iron (i.e., Fe VII–Fe X) in the model atmospheres, which have typically been neglected in previous studies of similar objects. The temperatures of the objects in our sample span a range over which different stages in this sequence dominate. Since Fe IV–Fe X have transitions that occur in the FUV and UV, the wavelength coverage of our spectral data is adequate to study these effects.

The ionization structures of iron for models in the temperature range of our sample (with similar mass-loss rates) are shown in Figure 2. The figures illustrate what ionization stages are dominant in various temperature regimes. For the cooler objects, Fe VI–Fe VII dominate. As $T_{\rm eff}$ increases, Fe VIII becomes dominant throughout the wind (at $T_{\rm eff} \gtrsim 100$ kK), and at the highest temperatures ($T_{\rm eff} \gtrsim 120$ kK) Fe IX becomes important in the inner winds layers. Useful iron diagnostics include the array of Fe V transitions occurring between 1350 and 1500 Å and the forest of Fe VI–Fe VII lines between 1250 and 1500 Å. Figure 3 demonstrates how the iron spectrum can be used as a diagnostic of wind parameters for NGC 1535.

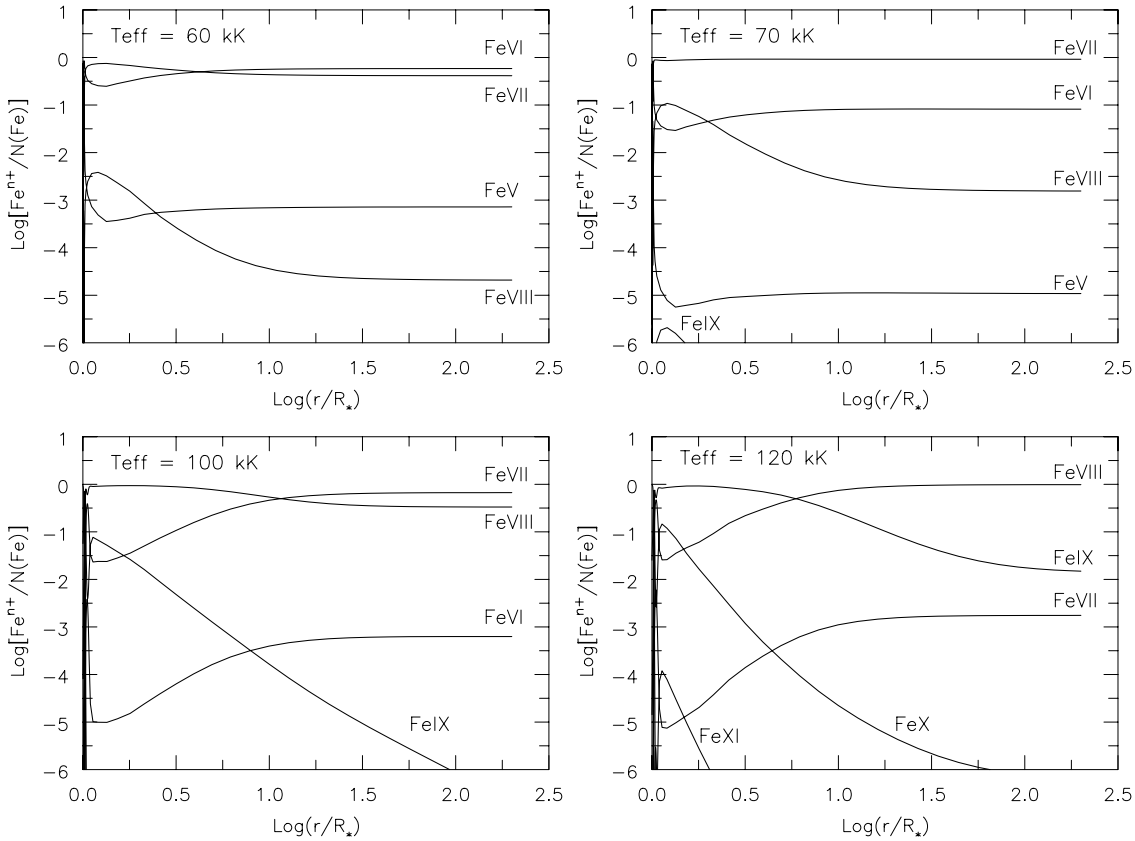

FIG. 2.—Ionization structure of iron for models spanning the temperature ranges of our objects, as a function of distance from the stellar surface. *Top*: Models with temperatures of our cooler objects ($T_{\rm eff} \simeq 60-70$ kK), where Fe VI–Fe VII dominate throughout the wind. *Bottom*: Models in the temperature range of our hotter objects ($T_{\rm eff} \simeq 100-130$ kK), where the higher ionization stages are dominant. These figures illustrate the sensitivity of the ionization structure of iron to $T_{\rm eff}$.

4.1.6. *Stellar Modeling Results*

Our model fits are shown in Figure 4. We now discuss our results for the individual objects, along with some notes. Our derived stellar parameters and a global discussion are given in § 5.

NGC 1535.—The strongest wind features (S VI, O VI, N V, O V, and C IV) of this O(H) star are all well fitted by our model using solar abundances. As discussed in § 4.1.5, the iron spectrum provides an additional constraint for this O(H) star, as at higher temperatures the Fe VII features are too strong (reducing $\dot{M}$ serves to weaken the noniron wind features to unacceptable levels).

Our derived parameters ($T_{\rm eff} = 66 \pm 5$ kK, $\log \dot{M} = -8.10 \pm 0.3\ M_\odot\ {\rm yr}^{-1}$) agree within the uncertainties with those of Koesterke et al. (2004), who model this object using a different wind code ($T_{\rm eff} = 70$ kK, $\log \dot{M} = -7.8\ M_\odot\ {\rm yr}^{-1}$). The temperature is about the same as that found by Méndez et al. (1988) in their plane-parallel analysis of optical spectra ($T_{\rm eff} = 58 \pm 5$ kK, $\log g = 4.3 \pm 0.2$). It is cooler than that derived by Tinkler & Lamers (2002), who reported the following parameters for NGC 1535: $T_{\rm eff} = 80$ kK, $R_* = 0.38\ R_\odot$, $\log L = 3.76\ \ L_\odot$, $\log g = 5.05$, $v_\infty = 1900$ km s^{-1}, and $\log \dot{M} = -8.7 \pm 0.7\ M_\odot\ {\rm yr}^{-1}$ ($R_t = 430^{+570}_{-280}$). Their mass-loss rate, which is about a factor of 4 lower than ours, was derived solely from O V λ1371, which we find is quite sensitive to $T_{\rm eff}$ in this temperature range.

IC 4776.—The nebular continuum for this object strongly contributes to the observed UV spectrum at longer wavelengths (§ 4.3). We are able to achieve fits of about the same

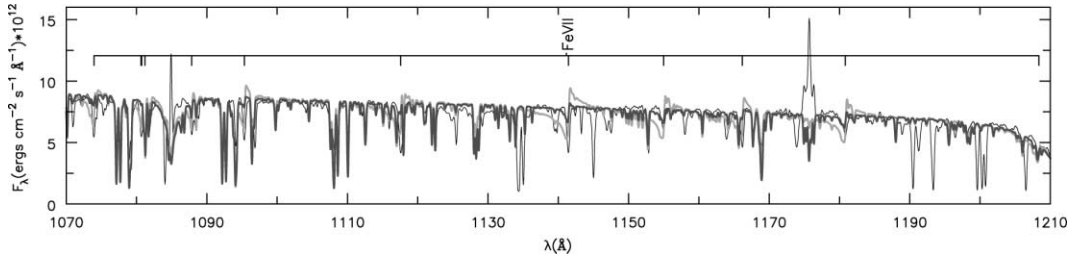

FIG. 3.—NGC 1535: Iron spectrum as a diagnostic. Observations of NGC 1535 are shown (*black line*), along with a model with $T_{\rm eff} \simeq 75$ kK, $\dot{M} \simeq 3 \times 10^{-8}\ M_\odot$ yr^{-1} (*light gray line*). This model displays an Fe VII spectrum stronger than the observations, indicating that a lower mass-loss rate and/or a different temperature is required. Our final model, with $T_{\rm eff} \simeq 65$ kK, $\dot{M} \simeq 1 \times 10^{-8}\ M_\odot$ yr^{-1} (*dark gray line*) provides a better fit. [*See the electronic edition of the Journal for a color version of this figure.*]

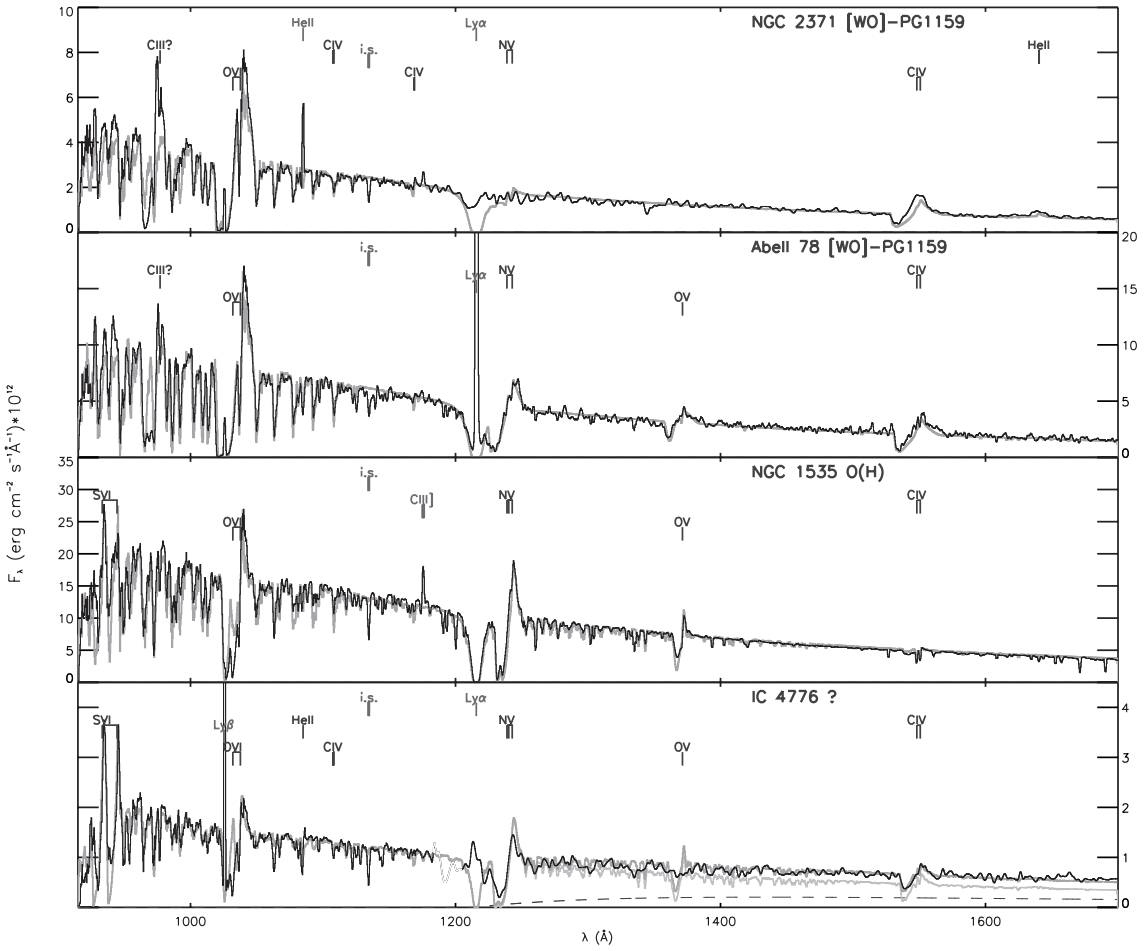

FIG. 4.—Model fits. The observations (*black lines*) have been unreddened using our values for E_{B-V} derived from the UV slope, and our models (*thick gray lines*) are also shown. In the case of IC 4776, the model nebular continuum (*dashed line*), and the stellar model (*thin gray line*) are summed together (*thick gray line*). The prominent wind features are marked with black labels, and strong nebular and interstellar features are marked with *gray* labels. The spectra have been convolved with a 0.75 Å Gaussian for clarity. [*See the electronic edition of the Journal for a color version of this figure.*]

quality for this object, using either our H-rich or H-deficient abundances, by adjusting $T_{\rm eff}$ within the range 55–70 kK and $\log \dot{M}$ within -7.85 ± 0.30 $M_\odot$ yr^{-1}, with the H-rich models yielding slightly better fits (it is our H-rich model that we present in the figures). O VI $\lambda\lambda$1032–1038 is a bit weak at $T_{\rm eff} \simeq 60$, but fits well at $T_{\rm eff} = 70$ kK. The S VI $\lambda\lambda$933–944 absorption is too strong in our presented model. It is better fitted with the lower limit of our mass-loss rate, but the other wind features are then a bit weak. Our models of either H-rich or H-deficient abundances overproduce O V λ1371, which is weak, at best, in the observations. Cooler models bring in (unobserved) O IV features, and lower mass-loss rates weaken all other features. Reducing the oxygen abundance to 1/100 solar brings the feature in line with observations, but then the O VI doublet in the FUV range is far too weak. Bouret et al. (2003) had difficulties fitting this feature in O dwarf stars, which have mass-loss rates of the order of 10^{-9} to 10^{-6} $M_\odot$ yr^{-1} and are cooler ($T_{\rm eff} \simeq 40$–50 kK). They found that a very clumped wind ($f = 0.01$) alleviated the problem somewhat.

Our mass-loss rates also agree with the predictions we obtained using the Vink et al. (2001) prescription (§ 5), which uses normal (i.e., non–He- or C-enriched) abundances. The low mass-loss rate of these objects and the dearth of diagnostics make the abundances difficult to constrain, and from our analysis, we cannot tell if IC 4776 is H-rich or H-deficient. Comparison with the evolutionary tracks (also see § 5) indicate that this objects is most probably an He burner.

IC 4776 has been classified as a [WC6] star (Feibelman 1999) and as a WELS (Tylenda et al. 1993). The [WC6] classification for IC 4776 was based on the equivalent width of C III λ2297. This classification is questionable for the following reasons. A [WC5] or [WC6] object should contain relatively strong C III features throughout its spectrum (e.g., Crowther et al. 1998; Hillier & Miller 1999), whereas the FUV/UV spectrum of IC 4776 is relatively featureless. The *FUSE* spectrum of this object shows high ionization features, such as O VI and S VI, indicating a state of higher ionization than one would expect in a [WC6] object.

A78.—The prominent wind lines of this object (O VI, N V, O V, and C IV) are all well reproduced by our model, with the exception of the strong P Cygni feature at the location of C III λ977. Koesterke & Werner (1998) also had problems reproducing this feature in A78 and speculated that neglected iron lines might sufficiently cool the outer layers of the (otherwise hot) wind to allow for the formation of C III. However, we have tested models accounting for ionization stages of iron up to Fe X and had no success (the dominant ionization stages in the model winds for these objects are Fe VIII and Fe IX). As iron is likely depleted in this object (see below), this is probably not the solution (although cooling from other species is possible).

Using a solar value for the iron abundance ([Fe] = 7.67), we could not simultaneously fit the iron spectrum and our other diagnostic lines. For any appreciable mass-loss rate, relatively strong (unobserved) iron P Cygni features are seen in models with temperatures spanning ~70–130 kK. For lower temperatures ($T_{\rm eff} \lesssim 95$ kK), the set of Fe VII lines shown in Figure 3 is seen. The hotter models display strong Fe VIII and/or Fe IX features. This supports the findings of Werner et al. (2003), who found A78 to have an iron abundance of at most ~0.03 solar. Using this iron abundance, the model spectrum agrees with the observations. Miksa et al. (2002) have also found iron deficiency in a large sample of PG 1159 stars, the supposed descendants of these transitional objects. Iron deficiencies in these objects may result when material in the He intershell is exposed to *s*-process nucleosynthesis during a thermally pulsating AGB or post-AGB phase (Lugaro et al. 2003; Herwig et al. 2003).

Koesterke (2001) determined $T_* = 115$ kK, $R_t = 45.2\ R_\odot$, and $v_\infty = 3750$ km s^{-1} for this object, with mass fractions for C, O, and N of 40%, 15%, and 2%, respectively. Our parameters are essentially the same (36%, 8%, and 1%), except we derive $v_\infty = 3200 \pm 50$ from fitting the C IV $\lambda\lambda$1248–1251. Werner et al. (2003) derived $T_{\rm eff} = 110$ kK and $\log g = 5.5$, also in line with our determinations.

A78 is the prototype [WC]–PG 1159 star (Hamann 1996; Koesterke & Werner 1998) and was originally placed in a transition phase between the [WR] and PG 1159 [i.e., O(C)] phases by Méndez (1991). Crowther et al. (1998) suggested a [WO1]–PG 1159 classification based on its high O VI λ3818/C IV λ5808 ratio. This object also falls into the category termed "O VI–type CSPNs," distinguished by Smith & Aller (1969) from the [WC] class for having O VI $\lambda\lambda$3811–3834 as one of its most prominent optical features. Our model parameters (derived solely in the FUV and UV spectral regions) adequately reproduce the optical wind features of A78.

A78 is also of interest because it belongs to a small group of PNs that have H-poor, dusty ejecta. These nebulae consist of an H-poor shell surrounded by an outer H-rich region, indicating a second ejection event of H-deficient material during the post-AGB phase (Medina & Peña 2000).

NGC 2371.—As can be seen in Figure 1, the FUV flux of this object is almost identical to that of A78, except that the wind lines are more conspicuous and broader, indicating a higher terminal velocity and mass-loss rate. The UV spectrum lacks O V, which, in our models, disappears for $T_{\rm eff} \gtrsim 115$–120 kK. There is a weak signature of N V $\lambda\lambda$1238–1243. Because of the low resolution of our data, it is unclear if its origin is nebular or stellar. If the latter is assumed, this feature weakens enough to fit the observations in our synthetic spectra for models with $T_{\rm eff} \gtrsim 125$ kK (it should be kept in mind we have assumed a mass fraction of $X_{\rm N} = 0.01$ for nitrogen). The iron spectrum further constrains the temperature to be $T_{\rm eff} \gtrsim 130$ kK, because the Fe IX features in the FUV are too strong for lower $T_{\rm eff}$. However, if one assumes that this object is iron-deficient, as is A78 (see § 4.1.6), this restriction is removed. As with A78, our models fail to reproduce the strong wind feature at 977 Å.

The low-resolution *IUE* spectrum shows He II λ1640, but the one high-resolution *IUE* spectrum available shows that at least part of the He II emission is nebular. Our upper limit to the mass-loss rate assumes that it is all stellar, and our lower limit assumes no stellar He II line. The high-resolution spectrum also reveals the C IV emission to be partly nebular. The absorption trough appears to be saturated (the high-resolution spectrum is underexposed, and hence extremely noisy, but around the stronger lines there is enough flux to see these details).

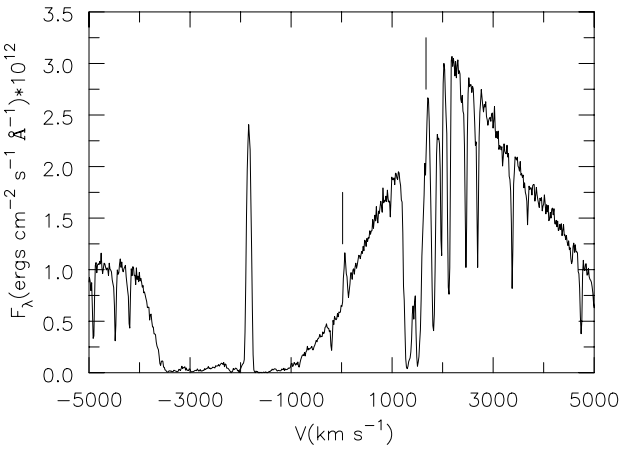

FIG. 5.—O VI $\lambda\lambda$1031.93, 1037.62 for NGC 2371, in velocity space around 1031.93 Å. The spectrum has been blueshifted to account for the measured radial velocity of the star of $v_r = +20.6$ km s^{-1} (Table 1). Marked is a narrow emission line at ~20 km s^{-1}, probably corresponding to the blue component of the doublet. We have also marked the corresponding position of the red component, assuming that it is velocity-shifted by the same amount. The red component seems to be present, but the absorption from H_2 prevents positive identification. Kaler et al. (1993) noticed similar narrow emission lines on top of the broad P Cygni profiles in optical O VI features.

Tylenda et al. (1993) classified NGC 2371 as a [WC3]. However, we find the ionization of the wind too high for such a classification. Our model parameters for NGC 2371 are close to those of A78 ([WO1]–PG 1159), with the former star being a bit hotter, with a denser wind. Their synthetic optical spectra are qualitatively similar, and so we suggest a [WO]–PG 1159 classification for NGC 2371, but at a higher state of ionization marked by the absence of O V and the presence of O VI. This classification needs to be confirmed with optical spectra, however.

Kaler et al. (1993) noted a peculiarity with the optical O VI emission features of this star: they consisted of two components, a broad, blended feature (with $v_\infty \simeq 3400$ km s^{-1}) and two resolved narrower features. It is the only known O VI planetary nebula nucleus (PNN) to display both the broad and narrow O VI features. They believed that these narrow features were associated with the wind rather than the nebula, because their long-slit CCD spectrum showed no extension of the narrow O VI features beyond the profile of the central star, confining the O VI formation zone to have a radius of ~2000 AU. It appears that the O VI $\lambda\lambda$1032–1038 for NGC 2371 also has this two-component structure, as shown in Figure 5. Close inspection reveals a narrow emission line superposed on the broad P Cygni profile, which could correspond to the blue component of the O VI doublet (at ~20 km s^{-1} in the rest wavelength of the star). The red feature may also be present, but H_2 absorption prevents a firm conclusion. These narrow O VI components may be evidence of shocked material in the nebula. Herald & Bianchi (2004) found similar (seemingly nebular) O VI features in the CSPN SMP LMC 62.

In their study of O VI PNNs, Stanghellini et al. (1995) have found a correlation between the strength of O VI $\lambda\lambda$3811–3834 and stellar luminosity. According to the models of our two transition stars, this holds true. Throughout our sample, the

TABLE 4
H_2 AND H I PARAMETERS

Star	Component[a]	log N	T	Note
NGC 2371.....	H I (IS+circ)	21.0	80	Not fitted
	H_2 (IS)	$18.0^{+0.7}_{-0.3}$	80	
	H_2 (circ)	$17.0^{+0.3}_{-0.7}$	300	
A78.....	H I (IS+circ)	21.1 ± 0.2	80	From Lyα
	H_2 (IS)	$19.7^{+0.3}_{-0.7}$	80	
	H_2 (circ)	$16.4^{+0.3}_{-0.7}$	300	
NGC 1535.....	H I (IS+circ)	20.8 ± 0.1	80	From Lyα
	H_2 (IS)	$18.7^{+0.3}_{-0.7}$	80	
	H_2 (circ)	$16.4^{+0.3}_{-0.4}$	400	
IC 4776.....	H I (IS+circ)	$21.4^{+0.3}_{-0.4}$	80	From Lyβ
	H_2 (IS)	$15.7^{+0.3}_{-0.7}$	80	
	H_2 (circ)	$15.7^{+0.3}_{-0.7}$	300	

[a] IS = ISM; circ = circumstellar region.

O VI $\lambda\lambda$1032–1038 feature grows stronger with increasing effective temperature and luminosity.

4.2. *Molecular and Atomic Hydrogen*

Absorption due to atomic and molecular hydrogen (H_2) along the sight line complicates the spectra of these objects in the *FUSE* range where numerous H_2 transitions from the Lyman ($B^1\Sigma_u^+ - X^1\Sigma_g^+$) and Werner ($C^1\Pi_u^\pm - X^1\Sigma_g^+$) sequences lie. Toward a CSPN, this sight-line hydrogen typically consists of interstellar and circumstellar components. Material comprising the circumstellar H I and H_2 presumably was ejected from the star earlier in its history (during the AGB phase) and is thus important from an evolutionary perspective. If this material is hot (e.g., $T \gtrsim 300$ K), a small column density [e.g., $\log N \sim 16$ cm^{-2}] of H_2 can lead to a complex absorption spectrum, obscuring the underlying stellar spectrum (see Fig. 5 of Herald & Bianchi 2004). It is therefore necessary to model the H I and H_2 characteristics to discern the underlying stellar spectrum. Our parameter determinations for sight-line H I and H_2 are listed in Table 4.

H_2 absorption effects are applied to the model spectrum in the following manner. For a given column density (N) and gas temperature (T), the absorption profile of each line is calculated by multiplying the line core optical depth (τ_0) by the Voigt profile $H(a, x)$ (normalized to unity), where x is the frequency in Doppler units and a is the ratio of the line-damping constant to the Doppler width (the "b" parameter). The observed flux is then $F_{\rm obs} = \exp[-\tau_0 H(a, x)] F_{\rm intr}$. To fit the H_2 spectrum of a given object, we first assume the presence of an interstellar component with $T = 80$ K (corresponding to the mean temperature of the interstellar medium (ISM); Hughes et al. 1971) and $v_{\rm turb} = 10$ km s^{-1}. The column density of this interstellar component is estimated by fitting the strongest transitions. If absorption features due to higher energy H_2 transitions are observed, a second, hotter (circumstellar) component is added (see example in Fig. 6). The temperature of the circumstellar component can be determined by the absence or presence of absorption features from transitions of different J-states, and the column density by fitting these features. Iterations between fitting the interstellar and circumstellar components are performed, as both contribute to the lower energy features. We note that our terminology of "circumstellar" and "interstellar" components is a simplification and basically indicates a "cool" component (assumed interstellar) and a "hot" component (assumed circumstellar). However, the column density derived for the cooler interstellar component may also include circumstellar H_2.

In the case of NGC 1535, the H_2 has been previously modeled by Bowers et al. (1995), using the $\sim$3 Å resolution Hopkins Ultraviolet Telescope. They found the data to be well fitted, employing either a one-component model of $T = 300$ K or a two-component model with $T = 144$ and 500 K. Their upper limit for the circumstellar H_2 column density was $\log N(H_2) = 18.4$ cm^{-2}. This is consistent with our findings, in which we have fitted the H_2 absorption (see § 4.2) using two components, a cool component [$T = 80$ K, $\log N(H_2) = 18.7$ cm^{-2}] and a hot component [$T = 400$ K, $\log N(H_2) = 16.7$ cm^{-2}], thanks to the higher resolution of the *FUSE* spectra.

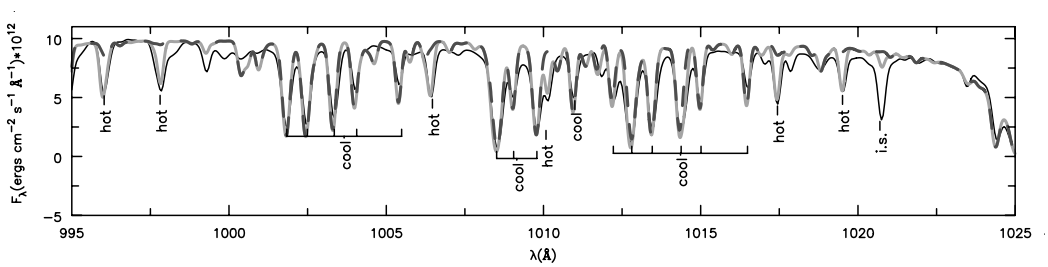

FIG. 6.—Fitting H_2. The *FUSE* spectrum of NGC 1535 is shown (*black line*), along with a stellar model with successive hydrogen absorption components applied (Table 4). The dashed line shows the stellar model with absorption from the cool ($T = 80$ kK) H I and H_2 components applied and the solid gray line that with absorption effects of the hot H_2 component ($T = 400$) H_2 applied. Features attributable to the hot and cool components, as well as strong interstellar absorption features, are labeled. The cool hydrogen absorption model is not sufficient to fit all the features, suggesting a hot H_2 gas associated with the nebula. [*See the electronic edition of the Journal for a color version of this figure.*]

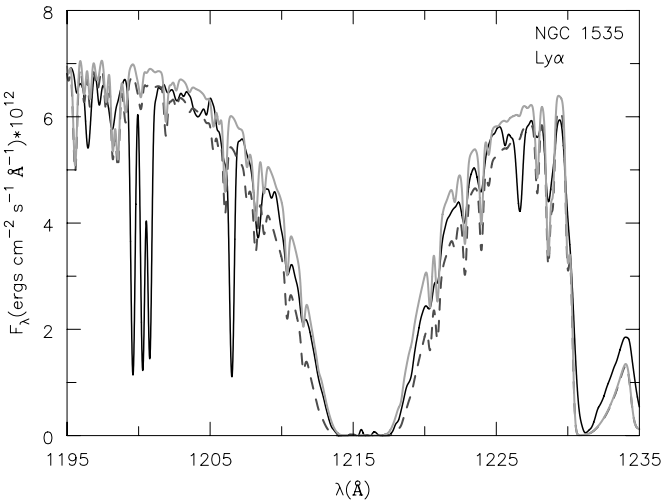

FIG. 7.—Fitting Lyα of NGC 1535. The Lyα profile in the STIS data (*black line*) and our stellar model with the absorption effects of different amounts of H I applied ($T = 80$ kK): column densities of $\log N = 20.8$, (*solid gray line*) and 21.0 cm^{-2} (*dashed line*). The models bracket the observations, so the sight-line column density can be well constrained to $\log N = 20.8 \pm 0.1$ cm^{-2}. [*See the electronic edition of the Journal for a color version of this figure.*]

H I column densities are determined in a similar fashion by fitting the profiles of the Lyα and/or Lyβ features (our primary diagnostic feature is indicated in Table 4). For A78 and NGC 1535, the available high-resolution data of the Lyα line enable the sight-line H I to be constrained tightly, as illustrated in Figure 7. For IC 4776 and NGC 2371, the low-resolution *IUE* spectra are inadequate for this purpose. For IC 4776, we use the blue side of the Lyβ profile, but for NGC 2371, the P Cygni absorption from the O VI doublet extends far enough blueward that Lyβ is obscured. We therefore simply assume an H I column density of 21.0 for this object for fitting purposes.

4.3. *Nebular Continuum*

Nebular characteristics, taken from the literature, are shown in Table 5. Also presented are nebular radii ($r_{\rm neb}$) and dynamic (kinematic) ages $\tau_{\rm dyn} = r_{\rm neb}/v_{\rm exp}$, calculated using the angular sizes from Table 1 and the distances from Table 6. Since some nebulae have angular diameter measurements in two dimensions, we used the average, listed as $\theta_{\rm adopt}$.

To determine if the nebula significantly contributes to the UV flux, nebular continuum emission models were computed accounting for two-photon, H and He recombination, and free-free emission processes. The continuum model parameters are the electron density (n_e), the electron temperature (T_e), the helium to hydrogen ratio (He/H), and the doubly ionized–to–singly ionized helium ratio (He^{2+}/He^{+}). The computed emissivity coefficient of the nebular gas was scaled as an initial approximation to the total flux at the Earth by deriving the emitting volume absolute Hβ flux F(Hβ), unreddened using $c_{\rm H\beta} = 1.475E_{B-V}$. If the nebula was not entirely contained within the aperture used for the observations, the continuum was scaled by an appropriate geometrical factor ($4A/\pi\theta^2$ or $4A/\pi\theta_A\theta_B$, where A is the area of the aperture in square arcseconds). Because the value of F(Hβ) is very uncertain, the continuum model was then rescaled to match the observed flux.

For NGC 2371, A78, and NGC 1535, the estimated nebular continuum fluxes are $\sim$1%, $\lesssim$0.1%, and $\lesssim$0.01%, respectively, of the observed flux between 1400 and 1500 Å. These fluxes do not significantly affect the modeling of the stellar spectra. However, the contribution of the nebular continuum emission to the UV spectra of IC 4776 is significant and is responsible for the shape of the observed spectrum at the longer UV wavelengths. This can be seen in Figure 8, which shows the UV spectrum of this object, along with our stellar and nebular continuum models.

4.4. *Reddening*

In Table 7, we list reddenings determined from the FUV/UV spectral slope, from our measured H I column densities, and from literature. We discuss each in turn.

For even the coolest objects of our sample, wavelengths above 912 Å lie in the Rayleigh-Jeans tail of the spectral energy distribution. This makes the slope of the FUV/UV continuum insensitive to $T_{\rm eff}$ and mainly dependent on the reddening toward the object. We have thus used the slope of the FUV/UV spectra to constrain E_{B-V} toward three of our objects, for which the nebular continuum contribution is negligible. In doing so, we have used the reddening law of Cardelli et al. (1989), assuming $R_V = 3.1$, the standard Galactic value. Although their work was originally valid only for wavelengths longer than 1250 Å, ongoing work has shown that the law may be safely extended through the *FUSE* range (G. Clayton 2001, private communication). In the case of IC 4776, the nebular continuum contamination in the UV (§ 4.3) hinders this method. However, the FUV spectrum is primarily stellar, and the determination of E_{B-V} was based on this range. The sum of the stellar and nebular components, and the derived E_{B-V}, fit well with the overall wavelength range (900–3000 Å).

Our values determined from the UV slope agree well with those determined from literature values of the logarithmic extinction (at Hβ) using the relation $c_{\rm H\beta} = 1.475E_{B-V}$. In all cases, the reddening is very small and does not affect the results of the stellar modeling.

TABLE 5
NEBULAR PARAMETERS AND ESTIMATED KINEMATIC AGES

Star	n_e[a] (cm^{-3})	T_e[a] (K)	$\log(F^{\rm obs}_{\rm H\beta})$[a] (ergs cm^{-2} s^{-1})	He/H[a]	He^{2+}/He^{+}[a]	$v_{\rm exp}$(O III)[a] (km s^{-1})	$\theta_{\rm adopt}$ (arcsec)	$r_{\rm neb}$ (pc)	$\tau_{\rm dyn}$ (kyr)
NGC 2371.....	1260 (1)	14,100 (2)	−10.99 (2)	0.11 (3)	0.688 (2)	42.5 (4)	40	0.15	3.3
A78.....	790 (5)	20,800 (2)	−12.04 (2)	0.110 (2)	1.61 (2)	27 (6)	107	0.42	15
NGC 1535.....	2100 (7)	10,800 (7)	−10.45 (2)	0.096 (2)	0.126 (2)	20 (6)	33	0.13	6.3
IC 4776.....	12000 (8)	8600 (2, 8)	−10.73 (2); −10.43 (9)	0.085 (2)	0.005 (2)	22 (10)	6	0.06	2.5

[a] References in parentheses; see below.

REFERENCES.—(1) Feibelman 1997; (2) Cahn et al. 1992; (3) Kaler et al. 1993; (4) Sabbadin 1984; (5) Medina & Peña 2000 (inner knots, upper limit); (6) Weinberger 1989; (7) Tylenda et al. 1991; (8) Phillips 1998; (9): adopted; see text; (10) Gesicki & Zijlstra 2000.

TABLE 6
DERIVED STELLAR PARAMETERS AND ADOPTED DISTANCES

Star	$T_{\rm eff}$[a] (kK)	R_t[a] ($R_\odot$)	v_∞[a] (km s^{-1})	D (kpc)	R_*[a] ($R_\odot$)	$\log L$[a] ($L_\odot$)	$\log \dot{M}$[a] ($M_\odot$ yr^{-1})	$\log \dot{M}$[b] ($M_\odot$ yr^{-1})	η[a]
NGC 2371.....	135^{+10}_{-15}	15^{+10}_{-5}	3700 ± 200	1.5[c]	0.09	$3.45^{+0.12}_{-0.20}$	-7.11 ± 0.30	-10.6	5.0
A78.....	113 ± 8	37^{+20}_{-15}	3200 ± 50	1.6[c]	0.19	$3.73^{+0.10}_{-0.13}$	$-7.33^{+0.36}_{-0.13}$	-9.3	1.4
NGC 1535.....	66 ± 5	200^{+100}_{-75}	1950 ± 50	1.6[d]	0.43	3.60 ± 0.13	-8.10 ± 0.30	-8.1	0.2
IC 4776	60^{+10}_{-5}	125^{+105}_{-45}	2300 ± 200	3.9[c]	0.35	$3.20^{+0.27}_{-0.15}$	-7.85 ± 0.30	-8.8	1.0

[a] From our spectral modeling.
[b] Predicted mass-loss rate for our derived parameters $T_{\rm eff}$, L, $\log g$, v_∞, using the prescription of Vink et al. (2001).
[c] Cahn et al. (1992).
[d] Sabbadin et al. (1984).

Finally, we list the reddenings implied by our measured column densities of H I (§ 4.2), using the relationship $\langle N({\rm H\ I})/E_{B-V}\rangle = 4.8 \times 10^{21}$ cm^{-2} mag^{-1} (Bohlin et al. 1978), which represents typical conditions in the ISM. This results in significantly higher reddenings than the other two methods, indicating that the derived column density includes a significant amount of *circumstellar* H I; apparently, the dust-to–H I ratio is smaller in the circumstellar region than in the ISM. This is similar to our findings for other CSPNs (Herald & Bianchi 2002, 2004).

5. RESULTS AND DISCUSSION

As discussed in § 4.1, values of $\log g$ were taken or estimated from previous works based on optical spectra (photospheric lines). From our spectral fitting process we determined the distance-independent parameters $T_{\rm eff}$, R_t, and v_∞. Once a distance was adopted, R_* was derived by scaling the model flux to the observations, and then L and $\dot{M}$ were determined. Distances to our objects found in the literature, derived by various methods, show large spreads (e.g., for NGC 1535, 0.8–3.1 kpc; Sabbadin et al. 1984). Most were determined from nebular relations, such as that of the nebular radius to ionized mass. Ciardullo & Jacoby (1999) have shown that, in comparison with distance determinations made from more reliable methods, such as spectroscopic parallax, statistical methods typically are off by a factor of 2 or more. With this in mind, our adopted distances from literature are shown in Table 6, along with the resulting parameters.

The results of comparing the effective temperatures and luminosities of our sample to the evolutionary tracks of Vassiliadis & Wood (1994) are shown in Table 8. They include the core mass (M_c, essentially the current mass), the initial mass of the progenitor ($M_{\rm init}$), the evolutionary age ($\tau_{\rm evol}$), and the gravity, derived using M_c and the radii (Table 6). NGC 1535, the H-rich object, was compared with the H-burning tracks and lies along the constant-luminosity phase. We used the He-burning tracks for NGC 2371 and A78, which both fall on the bend between the constant-luminosity phase and the WD cooling sequence, as appropriate for their transitional nature. At the temperature of IC 4776, the H-burning tracks extend down to luminosities of $\log L \gtrsim 3.5\ L_\odot$ (corresponding to the $M_{\rm init} = 1.0\ M_\odot$ track). The upper limit of our luminosity for IC 4776 ($\log L = 3.2^{+0.27}_{-0.15}\ L_\odot$) does not overlap with the H-burning tracks. The parameters of IC 4776 do, however, fall on the He-burning tracks, which we have used in this case. Which tracks were used are listed in Table 8.

In most cases, masses calculated using our derived radii and initially adopted gravities ($\log g = 5.5$ for A78 and NGC 2371, $\log g = 4.3$ for NGC 1535 and IC 4776; § 4.1.2) are unreasonably low (i.e., $\lesssim 0.5\ M_\odot$). Gravities computed using the track masses are higher than our adopted values in all cases. The gravities of NGC 2371 and A78 ($\log g = 6.3$ and 5.7, respectively) are good agreement with those of PG 1159 stars of similar temperatures from the 16 object sample of Miksa et al. (2002). Likewise, the gravities of NGC 1535 and IC 4776 ($\log g = 4.9$ and 5.1) are reasonable for CSPNs of these temperatures (e.g., Méndez et al. 1988). Models with these higher gravities resulted in only slight changes to the stellar parameters, within the errors quoted in Table 6. Therefore, we conclude that these higher gravities are more appropriate for our sample than those originally adopted from the literature.

For most of our objects, the dynamic ages (Table 5) are 2–4 times lower than the evolutionary ages. This is not unexpected, as the dynamic age is a lower limit to the post-AGB age, because the nebular expansion increases during the early

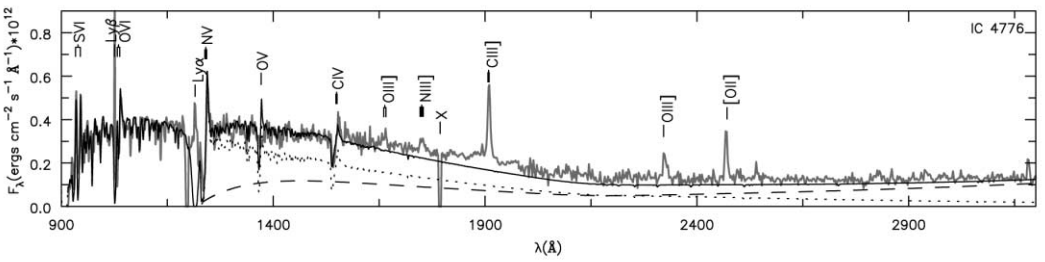

FIG. 8.—IC 4776. The observations are shown (*gray line*) along with our stellar (*dotted line*) and nebular continuum models (*dashed line*). The sum of both models is also shown (*solid black line*), demonstrating that the flux longward of Lyα (1215 Å) of this object is significantly affected by the nebular continuum. We have applied our molecular hydrogen absorption model (§ 4.2) to the stellar model and our atomic hydrogen absorption model to both the stellar and nebular models. In the FUV, the observations and models have been convolved with a 2 Å Gaussian for clarity.

TABLE 7
REDDENING PARAMETERS

Star	E_{B-V} (UV slope) (mag)	E_{B-V} ($c_{H\beta}$) (mag)	E_{B-V} (H I) (mag)
NGC 2371	0.070 ± 0.02	0.07[a]	...
A78	0.100 ± 0.02	0.12[b]	0.21
NGC 1535	0.055 ± 0.02	0.07[b]	0.13 ± 0.03
IC 4776	0.090 ± 0.02	0.07[b]	$0.52^{+0.52}_{-0.21}$

[a] Kaler et al. (1993).
[b] Cahn et al. (1992).

post-AGB phase and then levels off as the nucleus fades (see Sabbadin 1984; Bianchi 1992 and references therein). The exception is A78, which has a dynamic age larger than its evolutionary age ($\tau_{dyn} = 15$ kyr vs. $\tau_{evol} = 10$ kyr).

Vink et al. (2001) presented wind models that yield mass-loss rates for given stellar parameters, taking into account opacity shifts in the wind due to different ionization structures at different temperatures. They assume "normal" abundances—i.e., not He- or CNO-enriched. Although their prescriptions were derived from studies of the winds of (massive) O and B stars, we applied their prescription, using the derived parameters (T_{eff}, L, v_∞, and $\log g$) of our *low-mass* objects (Table 6) and solar metallicity. The results are listed in Table 6. The predicted mass-loss rate of NGC 1535 (which we fit with normal abundances) is the same as our measured value. For NGC 2371 and A78 (the H-deficient objects), the predicted mass-loss rates are many orders of magnitude lower than our values. This is probably due to the chemically enriched winds of these objects having much higher opacities. For IC 4776, a predicted mass-loss rate is an order of magnitude lower than our measured value results. This may be an indication that the wind of IC 4776 has some chemical enrichment, another indication that it may be an He burner.

The mass-loss rates of the H-deficient objects are about an order of magnitude larger than that of the H-rich object and have higher terminal velocities. The more powerful winds of the hotter objects are a consequence of the hydrogen deficiency of the atmosphere, which increases the opacity and thus the efficiency in converting radiative momentum flux into wind momentum flux. A measure of the efficiency of the wind at converting radiative momentum flux to wind momentum flux is the "performance number," $\eta = v_\infty \dot{M} c/L$ (Springmann 1994). The performance number basically measures how many times, on average, each photon scatters in the wind. Performance numbers above unity (the "single-scattering limit") are typical of stars with chemically enriched winds, such as WR objects. The performance numbers for our sample are also listed in Table 6 and show the H-rich object having the lowest η, while the two H-deficient objects are above the single-scattering limit. IC 4776 has a performance number of unity, again indicating that its wind may be chemically enriched.

6. CONCLUSIONS

We have performed an FUV/UV spectral analyses on four CSPNs that display combined absorption and wind line spectra, a sign that the winds of these objects are in the process of switching off. Two objects are H-deficient (NGC 2371 and A78), one is H-rich (NGC 1535), and for one our analysis is inconclusive (IC 4776). Thus, both channels of the CSPN phase are represented. We derived the stellar wind parameters of the sample PNs by modeling their FUV and UV spectra, where strong wind signatures are seen. NGC 1535 and A78 have been previously analyzed in the optical using plane-parallel models (Werner et al. 2003; Méndez et al. 1988), and the latter also with wind models (Koesterke & Werner 1998). Our parameters are in good agreement with the previous results.

The most striking feature in all the FUV spectra is the O VI doublet. In massive O-type stars, this ion originates from X-rays due to shocks in the radiatively driven winds (Bianchi & Garcia 2002). Because of the higher effective temperature of our sample CSPNs, we are able to fit this feature without the inclusion of X-rays.

Two objects have $T_{eff} \simeq 65$ kK, with $\dot{M} \sim 10^{-8}\ M_\odot\ \mathrm{yr}^{-1}$. NGC 1535 has been classified as a hydrogen-rich O(H) star on the basis of its optical spectrum, and we are able to match its FUV/UV spectrum using solar abundances. From the spectrum of IC 4776, we cannot constrain the abundances, but comparison with evolutionary tracks suggests that this object is an He burner. Our models for these objects show a jump in the ionization structure of the CNO elements (and S and P) between 55 and 70 kK. It is in this temperature range that Tinkler & Lamers (2002) find that H-rich CSPNs exhibit a large jump in $\dot{M}$ by an factor of 10–100, which they suspect is due to such a bistability jump. This supports the idea of Vink et al. (2001) that a bistability jump at such high temperatures may be due to CNO elements.

The two H-deficient objects A78 and NGC 1271 are significantly hotter ($T_{eff} > 110$ kK), with $\dot{M} \sim 10^{-7}\ M_\odot\ \mathrm{yr}^{-1}$. Our derived parameters for the [W01]–PG 1159 star A78

TABLE 8
DERIVED STELLAR PARAMETERS FROM EVOLUTIONARY TRACKS OF VASSILIADIS & WOOD (1994)

Star	Track	M_c ($M_\odot$)	M_{init} ($M_\odot$)	τ_{evol} (kyr)	$\log g$ (cm s^{-2})
NGC 2371	He	0.63	2	$\sim$13	6.3
A78	He	>0.63	>2.0	$\lesssim$10	5.7
NGC 1535	H	0.58	1.2	$\sim$15	4.9
IC 4776	He	0.57	1.0	$\sim$8	5.1

generally agree with those of past analyses. We derive similar parameters for NGC 2371 and suggest that it is a [WR]–PG 1159 star also, but its wind is more ionized and shows no O v features (a [WO0]–PG 1159?). We find evidence of iron deficiency in both of these objects, supporting the findings of Werner et al. (2003) in A78 and of Miksa et al. (2002) in PG 1159 stars. They lie on the bend in the theoretical evolutionary tracks between the constant-luminosity phase and the WD cooling sequence, having post-AGB ages of 10–15 kyr. For [WC] stars, it seems that as the star evolves away from the post-AGB phase through the [WC] sequence, the temperature and terminal velocity of the wind increase as the wind density decreases (Acker & Neiner 2003).

Except for A78, the post-AGB ages predicted by the evolutionary models are typically 2–4 times lower than their kinematic ages. However, kinematic ages are lower limits to the post-AGB age (as the expansion is slower in the initial phase); thus, the actual discrepancy may be smaller.

Our FUV/UV analysis has provided wind parameters for H-rich and H-deficient CSPNs at the stage in post-AGB evolution when the winds are fading. However, because a precise determination of the mass is not possible, the objects do not necessarily represent the same evolutionary sequence. This work has also provided information on the interstellar and circumstellar environment from our measurements of the column densities and temperatures of H I and H_2 along the sight lines. Our determinations of the H I column density and E_{B-V} imply that the relationship between these two quantities in the circumstellar (PN) environment of CSPNs differs from that of the ISM, having lower dust-to-gas ratios (probably because of the destruction of dust by the radiation field). The high resolution of the *FUSE* data allows us to detect hot H_2 associated with the nebulae. For all four objects in our sample, a single component of H_2 gas at typical ISM temperatures (i.e., $T \sim 80$ kK) was not adequate to fit the absorption spectrum. A second, hotter ($T \sim 300$ kK) component was necessary, which we assume to be associated with the circumstellar environment. With the advent of many *FUSE* observations of CSPNs, it is becoming apparent that hot circumstellar H_2 is not uncommon in PNs at quite different evolutionary stages: from old PNs with white dwarf nuclei (Herald & Bianchi 2002) to young, compact PNs (Herald & Bianchi 2004). The objects in this paper lie either along the constant-luminosity section of the post-AGB evolutionary tracks or on the transition bend to the WD cooling sequence and thus represent intermediate stages to the previously mentioned cases. Given the intense UV radiation fields emitted by the CSPNs, it is likely that the nebular H_2 exists in clumps, shielded by neutral and ionized hydrogen, as appears to be the case in the Helix Nebula (Speck et al. 2002).

We thank John Hillier for his help with the CMFGEN code and Stephan McCandliss for making his H_2 molecular data available. We are indebted to the members of the Opacity Project and Iron Project and to Bob Kurucz, for their continuing efforts to compute accurate atomic data, without which this project would not have been feasible. We are grateful to the referee, Klaus Werner, for his many constructive comments and suggestions. The SIMBAD database was used for literature searches. This work has been funded by NASA grants NAG5-9219 (NRA-99-01-LTSA-029), NAG5-10364, and NAG5-10364. The BEFS, STIS, and *IUE* data were obtained from the Multimission Archive (MAST) at the Space Telescope Science Institute (STScI). STScI is operated by the Association of Universities for Research in Astronomy, Inc., under NASA contract NAS5-26555.

APPENDIX

MODEL ATOMS

Ions and the number of levels and superlevels included in the model calculations are listed in Table 9. The atomic data come from a variety of sources, with the Opacity Project (Seaton 1987; Opacity Project Team 1995, 1997), the Iron Project (Pradhan et al. 1996; Hummer et al. 1993), Kurucz & Bell (1995),[2] and the Atomic Spectra Database at NIST Physical Laboratory being the principal sources. Many of the Kurucz data were obtained directly from CfA (Kurucz 1988, 2002). Individual sources of atomic data include the following: Zhang & Pradhan (1997), Bautista & Pradhan (1997), Becker & Butler (1995), Butler et al. (1993), Fuhr et al. (1988), Luo & Pradhan (1989), Luo et al. (1989), Mendoza (1983), C. Mendoza (1995, private communication), Mendoza et al. (1995), Nussbaumer & Storey (1983, 1984), Peach et al. (1988), P. J. Storey (1988, private communication), Tully et al. (1990), and Wiese et al. (1966, 1969). Unpublished work taken from the Opacity Project includes Fe VI data (PI K. Butler), Fe VIII data (PI Saraph and Storey), and Fe IX and Fe X data (PI C. Mendoza).

[2] See http://cfa-www.harvard.edu/amdata/ampdata/amdata.shtml.

TABLE 9
LEVELS AND SUPERLEVELS FOR MODEL IONS

Element	I	II	III	IV	V	VI	VII	VIII	IX	X	XI
H.....	20/30	1/1	...	...	...	...	...	...	...	...	...
He.....	40/45	22/30	1/1	...	...	...	...	...	...	...	...
C.....	...	...	30/54	13/18	1/1	...	...	...	...	...	...
N.....	...	...	...	29/53	13/21	1/1	...	...	...	...	...
O.....	...	...	...	29/48	41/78	13/19	1/1	...	...	...	...
Si.....	...	...	...	22/33	1/1	...	...	...	...	...	...
P	...	...	...	36/178	16/62	1/1	...	...	...	...	...
S	...	...	...	51/142	31/98	28/58	1/1	...	...	...	...
Fe.....	...	...	...	51/294	47/191	44/433	41/254	53/324	52/490	43/210	1/1

REFERENCES

Acker, A., & Neiner, C. 2003, A&A, 403, 659
Bautista, M. A., & Pradhan, A. K. 1997, A&AS, 126, 365
Becker, S. R., & Butler, K. 1995, A&A, 301, 187
Bianchi, L. 1992, A&A, 260, 314
Bianchi, L., & Garcia, M. 2002, ApJ, 581, 610
Bohlin, R. C., Savage, B. D., & Drake, J. F. 1978, ApJ, 224, 132
Bouret, J.-C., Lanz, T., Hillier, D. J., Heap, S. R., Hubeny, I., Lennon, D. J., Smith, L. J., & Evans, C. J. 2003, ApJ, 595, 1182
Bowers, C. W., Blair, W. P., Long, K. S., & Davidsen, A. F. 1995, ApJ, 444, 748
Butler, K., Mendoza, C., & Zeippen, C. J. 1993, J. Phys. B, 26, 4409
Cahn, J. H., & Kaler, J. B. 1971, ApJS, 22, 319
Cahn, J. H., Kaler, J. B., & Stanghellini, L. 1992, A&AS, 94, 399
Cardelli, J. A., Clayton, G. C., & Mathis, J. S. 1989, ApJ, 345, 245
Ciardullo, R., & Jacoby, J. H. 1999, ApJ, 515, 191
Crowther, P. A. 1999, in IAU Symp. 193, Wolf-Rayet Phenomena in Massive Stars and Starburst Galaxies, ed. K. A. van der Hucht, G. Koenigsberger, & P. R. J. Eenens (San Francisco: ASP), 116
Crowther, P. A., De Marco, O., & Barlow, M. J. 1998, MNRAS, 296, 367
Crowther, P. A., Dessart, L., Hillier, D. J., Abbott, J. B., & Fullerton, A. W. 2002, A&A, 392, 653
De Marco, O., & Soker, N. 2002, PASP, 114, 602
Feibelman, W. A. 1997, ApJS, 112, 193
———. 1999, ApJ, 519, 726
Fuhr, J. R., Martin, G. A., & Wiese, W. L. 1988, Atomic Transition Probabilities: Iron through Nickel (J. Phys. Chem. Ref. Data, Vol. 17, Suppl. 4)
Gesicki, K., & Zijlstra, A. A. 2000, A&A, 358, 1058
Górny, S. K., & Tylenda, R. 2000, A&A, 362, 1008
Gray, D. F. 1992, The Observation and Analysis of Stellar Photospheres (Cambridge: Cambridge Univ. Press)
Hamann, W.-R. 1996, Ap&SS, 238, 31
Hamann, W.-R., Koesterke, L., & Wessolowski, U. 1993, A&A, 274, 397
Herald, J. E., & Bianchi, L. 2002, ApJ, 580, 434
———. 2004, ApJ, in press
Herald, J. E., Hillier, D. J., & Schulte-Ladbeck, R. E. 2001, ApJ, 548, 932
Herwig, F. 2001, Ap&SS, 275, 15
Herwig, F., Lugaro, M., & Werner, K. 2003, in IAU Symp. 209, Planetary Nebulae: Their Evolution and Role in the Universe, ed. S. Kwok, M. Dopita, & R. Sutherland (San Francisco: ASP), 85
Hillier, D. J., Lanz, T., Heap, S. R., Hubeny, I., Smith, L. J., Evans, C. J., Lennon, D. J., & Bouret, J. C. 2003, ApJ, 588, 1039
Hillier, D. J., & Miller, D. L. 1998, ApJ, 496, 407
———. 1999, ApJ, 519, 354
Hughes, M. P., Thompson, A. R., & Colvin, R. S. 1971, ApJS, 23, 323
Hummer, D. G., Berrington, K. A., Eissner, W., Pradhan, A. K., Saraph, H. E., & Tully, J. A. 1993, A&A, 279, 298
Hurwitz, M., et al. 1998, ApJ, 500, L1
Kaler, J. B., Stanghellini, L., & Shaw, R. A. 1993, A&A, 279, 529
Koesterke, L. 2001, Ap&SS, 275, 41
Koesterke, L., Dreizler, S., & Rauch, T. 1998, A&A, 330, 1041
Koesterke, L., & Werner, K. 1998, ApJ, 500, L55
Koesterke, L., Werner, K., Kruk, J. W., & Lanz, T. 2004, in ASP Conf. Ser. 313, Asymmetric Planetary Nebulae III, ed. M. Meixner, J. H. Kastner, B. Balick, & N. Soker (San Francisco: ASP), in press (astro-ph/0402049)
Kudritzki, R.-P., & Puls, J. 2000, ARA&A, 38, 613
Kudritzki, R.-P., Puls, J., Lennon, D. J., Venn, K. A., Reetz, J., Najarro, F., McCarthy, J. K., & Herrero, A. 1999, A&A, 350, 970
Kurucz, R. L. 1988, in Trans. IAU, XXB, ed. M. McNally (Dordrecht: Kluwer), 168
———. 2002, in AIP Conf. Proc. 636, Atomic and Molecular Data and Their Applications, ed. D. R. Schultz, P. S. Krstic, & F. Ownby (Melville: AIP), 134
Kurucz, R. L., & Bell, B. 1995, CD-ROM 23, Atomic Line Data (Cambridge: SAO)
Lugaro, M., Herwig, F., Lattanzio, J. C., Gallino, R., & Straniero, O. 2003, ApJ, 586, 1305
Luo, D., & Pradhan, A. K. 1989, J. Phys. B, 22, 3377
Luo, D., Pradhan, A. K., Saraph, H. E., Storey, P. J., & Yu, Y. 1989, J. Phys. B, 22, 389
Medina, S., & Peña, M. 2000, Rev. Mexicana Astron. Astrofìs., 36, 121
Méndez, R. H. 1991, in IAU Symp. 145, Evolution of Stars: The Photospheric Abundance Connection, ed. G. Michaud & A. Tutukov (Dordrecht: Kluwer), 375
Méndez, R. H., Kudritzki, R. P., Herrero, A., Husfeld, D., & Groth, H. G. 1988, A&A, 190, 113
Mendoza, C. 1983, in IAU Symp. 103, Planetary Nebulae, ed. D. R. Flower (Dordrecht: Reidel), 143
Mendoza, C., Eissner, W., Le Dourneuf, M., & Zeippen, C. J. 1995, J. Phys. B, 28, 3485
Miksa, S., Deetjen, J. L., Dreizler, S., Kruk, J. W., Rauch, T., & Werner, K. 2002, A&A, 389, 953
Moos, H. W., et al. 2000, ApJ, 538, L1
Napiwotzki, R. 1999, A&A, 350, 101
Nussbaumer, H., & Storey, P. J. 1983, A&A, 126, 75
———. 1984, A&AS, 56, 293
Opacity Project Team. 1995, The Opacity Project, Vol. 1 (Bristol: IoP)
———. 1997, The Opacity Project, Vol. 2 (Bristol: IoP)
Owocki, S. P., Castor, J. I., & Rybicki, G. B. 1988, ApJ, 335, 914
Owocki, S. P., Cranmer, S. R., & Blondin, J. M. 1994, ApJ, 424, 887
Parthasarathy, M., Acker, A., & Stenholm, B. 1998, A&A, 329, L9
Peach, G., Saraph, H. E., & Seaton, M. J. 1988, J. Phys. B, 21, 3669
Phillips, J. P. 1998, A&A, 340, 527
Pradhan, A. K., Zhang, H. L., Nahar, S. N., Romano, P., & Bautista, M. A. 1996, BAAS, 189, 72.11
Sabbadin, F. 1984, A&AS, 58, 273
Sabbadin, F., Bianchini, A., & Hamzaoglu, E. 1984, A&A, 136, 193
Sahnow, D. J., et al. 2000, ApJ, 538, L7
Schmutz, W., Hamann, W.-R., & Wessolowski, U. 1989, A&A, 210, 236
Seaton, M. J. 1987, J. Phys. B, 20, 6363
Smith, L. F., & Aller, L. H. 1969, ApJ, 157, 1245
Speck, A. K., Meixner, M., Fong, D., McCullough, P. R., Moser, D. E., & Ueta, T. 2002, AJ, 123, 346
Springmann, U. 1994, A&A, 289, 505
Stanghellini, L., Kaler, J. B., Shaw, R. A., & di Serego Alighieri, S. 1995, A&A, 302, 211
Tinkler, C. M., & Lamers, H. J. G. L. M. 2002, A&A, 384, 987
Tully, J. A., Seaton, M. J., & Berrington, K. A. 1990, J. Phys. B, 23, 3811
Tylenda, R., Acker, A., & Stenholm, B. 1993, A&AS, 102, 595
Tylenda, R., Acker, A., Stenholm, B., Gleizes, F., & Raytchev, B. 1991, A&AS, 89, 77
Tylenda, R., Siódmiak, N., Górny, S. K., Corradi, R. L. M., & Schwarz, H. E. 2003, A&A, 405, 627
Vassiliadis, E., & Wood, P. R. 1994, ApJS, 92, 125
Vink, J. S., de Koter, A., & Lamers, H. J. G. L. M. 2001, A&A, 369, 574
Weinberger, R. 1989, A&AS, 78, 301
Werner, K. 2001, Ap&SS, 275, 27
Werner, K., Dreizler, S., Koesterke, L., & Kruk, J. W. 2003, in IAU Symp. 209, Planetary Nebulae: Their Evolution and Role in the Universe, ed. S. Kwok, M. Dopita, & R. Sutherland (San Francisco: ASP), 239
Wiese, L. L., Smith, M. W., & Glennon, B. M. 1966, Atomic Transition Probabilities, Vol. 1 (NSRDS-NBS 4; Washington: GPO)
Wiese, L. L., Smith, M. W., & Miles, B. M. 1969, Atomic Transition Probabilities, Vol. 2 (NSRDS-NBS 22; Washington: GPO)
Zhang, H. L., & Pradhan, A. K. 1997, A&AS, 126, 373